Phosphorene oxides: Bandgap engineering of phosphorene by oxidation

A. Ziletti,[1,*] A. Carvalho,[2] P. E. Trevisanutto,[2] D. K. Campbell,[3] D. F. Coker,[1] and A. H. Castro Neto[2,3]
[1]*Department of Chemistry, Boston University, 590 Commonwealth Avenue, Boston Massachusetts 02215, USA*
[2]*Centre for Advanced 2D Materials and Graphene Research Centre, National University of Singapore, 6 Science Drive 2, 117546, Singapore*
[3]*Department of Physics, Boston University, 590 Commonwealth Avenue, Boston Massachusetts 02215, USA*
(Received 28 October 2014; revised manuscript received 20 January 2015; published 6 February 2015)

We show that oxidation of phosphorene can lead to the formation of a new family of planar (two-dimensional) and tubular (one-dimensional) oxides and suboxides, most of them insulating. This confers to black phosphorus a native oxide that can be used as barrier material and protective layer. Furthermore, the bandgap of phosphorene oxides depends on the oxygen concentration, suggesting that controlled oxidation can be used as a means to engineer the bandgap. For the oxygen saturated composition, P_2O_5, both the planar and tubular phases have a large bandgap energy of about 8.5 eV and are transparent in the near UV. These two forms of phosphorene oxides are predicted to have the same formation enthalpy as O′-P_2O_5, the most stable of the previously known forms of phosphorus pentoxide.

DOI: 10.1103/PhysRevB.91.085407 PACS number(s): 73.20.At, 73.61.Cw, 73.61.Ng

I. INTRODUCTION

Phosphorene, a single layer of black phosphorus, is a unique two-dimensional semiconductor with a nearly direct gap in the visible range [1,2]. It stands out among the family of two-dimensional (2D) materials for its orthorhombic waved structure with superior flexibility and small Young's modulus [3], allowing for strain-driven band-structure engineering [1]. From the point of view of electronic and optoelectronic applications, it features high carrier mobility and on-off ratio [4,5], as well as a giant photoresponse in the IR and UV [6].

In contrast to graphene, phosphorene is prone to oxidation [7], which usually leads to degradation of the structure and electronic properties [8–10]. At present, oxidation is avoided by encapsulating with polymers or other two-dimensional materials, e.g., graphene or boron nitride [8].

However, there are indications that a phosphate layer grown in a controlled way could be used as a protective layer or even as a functional material on its own. Black phosphorus oxidizes on the surface, seemingly leaving the deepest layers intact. The nonuniform degradation pattern normally observed, showing as dark patches on the optical microscope image, seems to require the interaction with water [11,12], even though energy-loss spectra shows P_xO_y still grows in oxygen-only atmosphere [13]. In this article, we show that phosphorene oxides and suboxides can exist in monolayer form, suggesting that there is an opportunity for growth of single-layer or few-layer native oxide at the black phosphorus surface.

The existence of an insulating native oxide is an added advantage for phosphorene.

Similarly to phosphate glasses [14], monolayer P_2O_5 is transparent in the near UV, preserving the optical properties of underlying phosphorene. Furthermore, since such a P_2O_5 coating is saturated with oxygen, it prevents oxygen molecules from reaching the pristine phosphorene layers beneath.

Bulk P_2O_5 has at least three known planar crystalline polymorphs—a molecular solid [15] (with P_4O_{10} structural units) and two orthorhombic phases [16,17], as well as an amorphous phase [18,19].

The thermodynamically most stable form (O′-P_2O_5) is a layered structure belonging to the *Pnma* space group [17]. A monolayer phase, different from the one reported here, has also been proposed by a recent theoretical study [20].

In this article, we show that suboxides (P_4O_n, $n < 10$) also exist in a variety of layered forms, most of them insulating, with bandgaps that depend on the oxygen concentration. This offers the possibility of using oxidation as a means to engineer the bandgap of phosphorene.

The article is organized as follow: after presenting the computational methodology, we describe the structure and energetics of phosphorene oxides; then, we consider their electronic properties and finally their vibrational spectra.

II. COMPUTATIONAL DETAILS

All first-principle calculations are based on the framework of density functional theory (DFT), as implemented in the QUANTUM ESPRESSO package [21]. We use the PBE [22], PBEsol [23], and HSE06 [24] (HSE hereafter) approximations for the exchange and correlation energy. The PBEsol functional is preferred over PBE because it cures the systematic tendency of PBE to overestimate equilibrium lattice constants of solids [23]. The HSE functional, with its fraction of screened short-ranged Hartree–Fock exchange, yields reasonably accurate predictions for energy bandgaps in semiconductors [25–27]. Unless otherwise stated, all quantities reported (e.g., energies, bond lengths, and bond angles) are obtained with the PBEsol functional. For PBEsol and PBE calculations the electron-ion interaction is described by using the projector-augmented wave (PAW)[28] approach, while norm-conserving Troullier–Martins pseudopotentials [29] are employed in HSE calculations. We use a plane-wave basis set with kinetic-energy cutoffs of 70 Ry (280 Ry) to describe the electronic wave functions (charge density). Vibrational properties including Raman and infrared spectra are calculated

*Corresponding author: ziletti@bu.edu

with density functional perturbation theory [30] (DFPT) and the PBEsol functional. The Brillouin zone is sampled using a Γ-centered $10 \times 8 \times 1$ Monkhorst–Pack (MP) grid [31] for all but the vibrational calculations, for which a finer $15 \times 12 \times 1$ grid is employed. A supercell periodicity of 16 Å in the direction perpendicular to the monolayer is used to avoid spurious interactions between replicas of the system. For each oxygen concentration, tens of different configurations are used as starting points for optimization. Then, lattice geometries and atomic positions are relaxed until the forces on each atom are less than 10^{-3} eV/Å and the pressure is less then 1 kbar, except for the HSE calculations, where we use the PBE (with norm-conserving pseudopotentials) lattice parameters. The tetrahedron smearing method [32] is used with a Gaussian broadening of 0.04 eV and a $12 \times 9 \times 1$ MP grid in the density of states (DOS) calculations. However, local and semilocal DFT functionals (such as PBE and PBEsol) are known to underestimate the bandgap because of their missing derivative discontinuity in the exchange-correlation energy across the gap [33,34]. The inclusion of a fraction of exact nonlocal short-ranged Hartree–Fock exchange, as done in HSE, partially cures this shortcoming, giving bandgaps in better agreement with experiment [24,27]. Thus, we use HSE to calculate the bandgap energy.

To further validate the HSE results, we calculate the bandgap of pristine phosphorene and the two phosphorene oxides (p-P_4O_{10} and t-P_4O_{10}) by using the GW approximation to the electron self-energy within the generalized plasmon pole model [35,36]. The GW method is state of the art for evaluating quasiparticle bandgaps since it gives values in very good agreement with experiment (typically within 0.2 eV) for a large variety of systems and a broad range of bandgaps [37]. The GW calculations are performed in two stages. First, relaxed lattice geometries, equilibrium atomic positions, and the electronic ground state are obtained from a DFT calculation with the PBE functional and Troullier–Martins pseudopotentials [29]. Then, the DFT Kohn–Sham orbitals and energies are used to construct both the electronic Green's function, G, and the dynamically screened interaction, W, to evaluate the quasiparticle self-energy $\Sigma \approx iGW$. This method is commonly referred to as G_0W_0. To achieve convergence in our GW calculations we follow the procedure proposed by Malone and Cohen [38]. For pristine phosphorene, we use 370 bands to evaluate the dielectric matrix ϵ and the self-energy Σ, employing an energy cutoff ϵ_{cutoff} of 12 Ry for the dielectric matrix and a $24 \times 20 \times 1$ MP grid; convergence was, however, checked with up to 1024 bands and by using ϵ_{cutoff} up to 20 Ry. For the two phosphorene oxides (p-P_4O_{10} and t-P_4O_{10}) we use an energy cutoff ϵ_{cutoff} of 8 Ry for the dielectric matrix, and 800 and 896 bands to evaluate ϵ and Σ, respectively. A $7 \times 4 \times 1$ grid for p-P_4O_{10} and a $4 \times 6 \times 1$ grid for t-P_4O_{10} are employed. Convergence was checked by including up to 1792 bands and increasing ϵ_{cutoff} up to 20 Ry. For all the GW calculations we use a supercell of 20 Å in the direction perpendicular to the monolayers and a slab-truncation of the Coulomb potential [39]. The GW calculations are performed with the ABINIT code [40]. Additional details on the convergence study are given in the supplemental material [41]. With these parameters, we conservatively estimate the errors in our GW bandgaps at 0.05 eV for pristine phosphorene and 0.1 eV for p-P_4O_{10} and t-P_4O_{10}.

III. RESULTS AND DISCUSSION

A. Crystal structure

First we describe the new family of phosphorene oxides (POs) found in this study. These are obtained by adding oxygen atoms to phosphorene, while preserving the rectangular symmetry of the lattice vectors. We considered all compounds P_4O_n with n between 1 and 10. The maximum oxygen concentration of 250%, or ten oxygen atoms per unit cell, corresponds to the stoichiometry of phosphorus pentoxide (P_2O_5 or P_4O_{10}), whose known polymorphs [42] were mentioned in the introduction.

For each oxygen concentration, we use tens of different starting points corresponding to different O atom arrangements in the pristine phosphorene lattice. After lattice relaxation and geometry optimization, numerous metastable phosphorous oxide (PO) structures are identified. We find that, for each oxygen concentration, the most stable POs can always be divided into two very distinctive classes: planar (2D) and tubular [one-dimensional (1D)] forms. For convenience, we refer to the planar forms as p-P_4O_n and to the tubular forms as t-P_4O_n, where n is the number of oxygen atoms in the unit cell. We also identify surface forms s-P_4O_n. Some representative structures are depicted in Fig. 1.

Analysis of the local oxygen atom environments that are common to both p-P_4O_n and t-P_4O_n forms presented in Fig. 1 indicates that all the PO structures identified exhibit two P–O motifs: the dangling and bridging oxygen motifs shown in Fig. 2.

The dangling oxygen motif, represented in Fig. 2(a), consists of an O atom that forms a bond with only one P atom. The phosphorus lone pair is attracted towards the more electronegative oxygen atom, giving rise to an excess of negative charge localized on the O atom [Fig. 2(a)]. The P–O bond is short, strong, and polar with bond lengths ranging from 1.44 Å to 1.51 Å depending on phosphorus oxidation number and local environment [43]. Similar to what has been found for dangling oxygens on a phosphorene surface [7], in the PO forms identified here, the P=O bonds always point away from

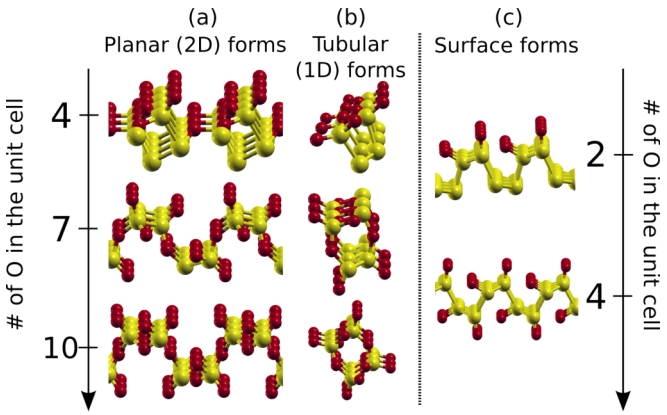

FIG. 1. (Color online) Representative structures of phosphorene oxides.

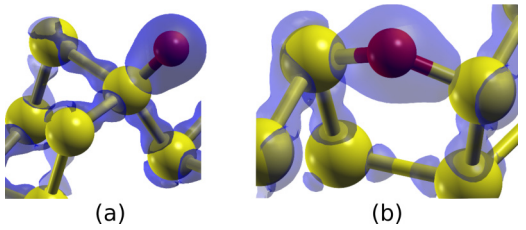

FIG. 2. (Color online) Examples of charge density distribution in recurrent motifs in phosphorene oxides: (a) dangling oxygen, (b) bridging oxygen. The isosurfaces correspond to 1/10 of the total charge density.

the zigzag ridge in which they are chemisorbed, minimizing Coulomb repulsion between the oxygen p orbitals.

The average P=O bond length decreases monotonically as the number of oxygens linked to the phosphorus involved in the bond increases. Let $P^{(n)}$ be a phosphorus atom that is linked to n oxygens, where $n = 1, \ldots, 4$. With this notation $P^{(1)}$=O defines a double bond in which a phosphorus is linked to only one oxygen, as shown, for example, in Fig. 2(a). The average P=O bond lengths for the sequence of $P^{(n)}$ configurations are given in Table I for the planar and tubular forms. The longest P=O bond is found for $n = 1$ (where the P atom establishes a P=O bond and three P–P bonds); conversely, the shortest P=O bonds are found in p-P_4O_{10} and t-P_4O_{10} ($n = 4$), where the phosphorus atom is bonded to four oxygens. This monotonic decrease in the P=O bond length with increasing oxygen connectivity has an analog in the molecular solid series P_4O_m ($m = 6$ to 10) [44–46].

In the bridge motif, as the name indicates, the oxygen atom bridges two P atoms, occupying a position close to a P–P bond center [Fig. 2(b)]. The electron density is mostly distributed on the two P–O bonds, and only a moderate electron density accumulation is observed on the oxygen. Therefore, we expect a much stronger Coulomb repulsion between dangling oxygens than bridging oxygens, especially for high O concentrations. The P–O bond lengths in this case are between 1.61 and 1.78 Å, with this wide range arising from different strain interactions and lattice distortions depending on the oxygen concentration.

Bridging oxygens can either bond with P atoms from the same or from different zigzag ridges, therefore forming intraridge [e.g., B or C in Fig. 3(b)] or inter-ridge [e.g., D in Fig. 3(b)] bridge structures. In particular, inter-ridge bridges are essential for the formation of the planar forms because they effectively link different ridges that would otherwise separate

TABLE I. Average bond lengths for various O linkages in planar and tubular forms (Å).

	Planar		Tubular	
	PBE	PBEsol	PBE	PBEsol
$P^{(1)}$=O	1.502	1.508	1.481	1.477
$P^{(2)}$=O	1.478	1.476	1.470	1.466
$P^{(3)}$=O	1.463	1.459	1.461	1.458
$P^{(4)}$=O	1.449	1.445	1.450	1.447

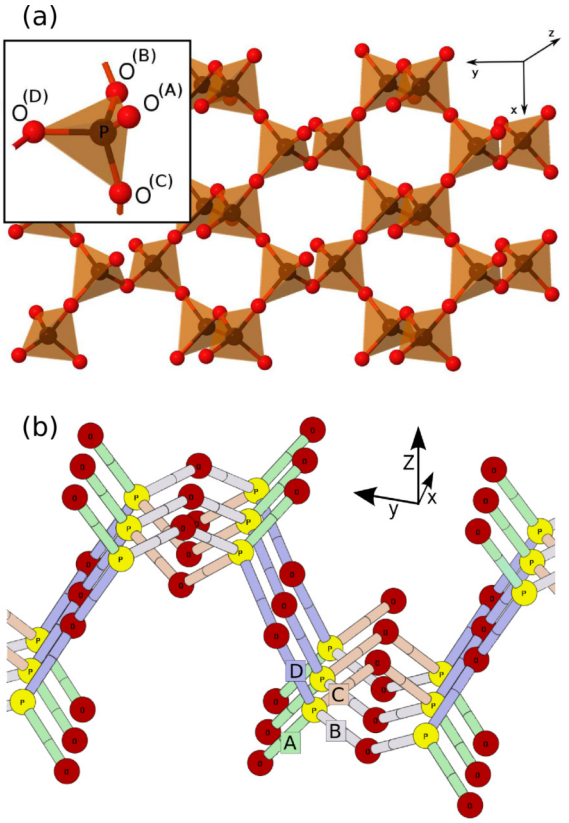

FIG. 3. (Color online) Crystal structure of p-P_4O_{10} (a) Top view. The quasitetrahedral PO_4 unit is shown in the inset. (b) Profile view. The four colors indicate four different bond lengths (A, B, C, D). Bonds with the same color are identical.

and form 1D tubular chains. The formation of oxygen bridges increases the lattice parameters considerably, resulting in deformations as large as 90% relative to pristine phosphorene for the maximally oxidized forms (see Table II).

Dangling and bridging oxygens can occupy numerous positions in the lattice, giving rise to a manifold of metastable, nearly degenerate structures. In the following we examine in detail the most stable POs obtained for maximum oxygen concentration: the planar p-P_4O_{10} and the tubular t-P_4O_{10} forms. These are shown in Figs. 3 and 4, respectively.

TABLE II. Lattice parameters (a,b) and deformations relative to pristine phosphorene for representative POs.

System	XC	a (Å)	b (Å)	Δa (%)	Δb (%)
Phosphorene	PBE	3.30	4.62	–	–
Phosphorene	PBEsol	3.28	4.45	–	–
p-P_4O_{10}	PBE	4.48	6.79	36	47
p-P_4O_{10}	PBEsol	4.41	6.75	34	51
t-P_4O_{10}	PBE	6.40	4.63	93	0.2
t-P_4O_{10}	PBEsol	6.28	4.58	91	2.9
s-P_4O_2	PBE	3.46	5.05	4.8	9.3
s-P_4O_2	PBEsol	3.41	4.37	3.9	−1.8
s-P_4O_4	PBE	3.64	5.11	10.3	10.6
s-P_4O_4	PBEsol	3.57	4.85	8.2	9.0

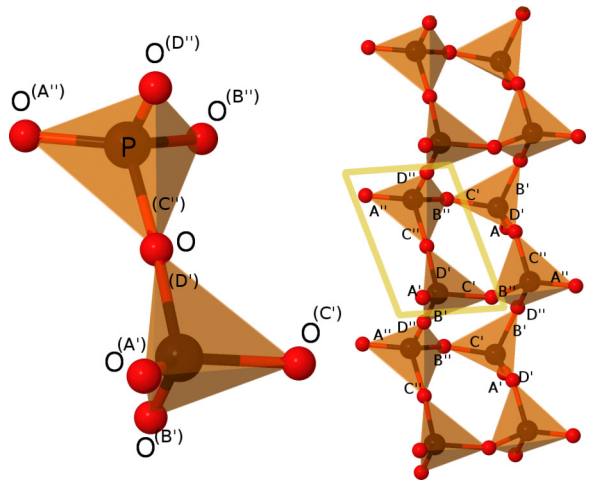

FIG. 4. (Color online) Single tubular chain of t-P_4O_{10}. The two inequivalent quasitetrahedral PO_4 units forming this tubular PO are shown on the left side.

The planar p-P_4O_{10} is a waved structure, like the parent phosphorene. It can be built by placing an oxygen atom near each bond center and near each lone pair. The space group is $Cm(C_s^3)$, and the unit cell contains four phosphorus and ten oxygen atoms. There are four inequivalent P–O bonds, three of which connect the phosphorus atom with bridging oxygens [B,C,D in Fig. 3(b)], while the forth links the phosphorus to a dangling oxygen [A in Fig. 3(b)]. The respective bond lengths are given in Table III. To minimize Coulomb repulsion, the bridging oxygens between P atoms in the same zigzag ridge alternate up and down buckling, forming two rows parallel to the x direction and separated by 1.23 Å in the z direction [see bonds C and B in Fig. 3(b)], one row being above and the other below the x-y plane passing through the two P atoms in the zigzag ridge.

Alternatively p-P_4O_{10} can be seen as consisting of identical quasitetrahedral PO_4 units, forming a network of vertex-sharing tetrahedra [Fig. 3(a)]. The bond lengths of the PO_4 tetrahedra are listed in Table III. The deviations from the ideal tetrahedral bond angles (109.5°) can be straightforwardly explained in the framework of valence-shell electron pair repulsion (VSEPR) theory [47–49]. The more polar P–$O^{(A)}$ bond repels the less polar other P–O bonds, causing larger bond angles relative to the idealized tetrahedral geometry [49].

The planar p-P_4O_{10} structure (shown in Fig. 3) is entirely different from the layered O′-P_2O_5 form previously reported by several experimental studies (see, for example, Ref. [17]), shown in Fig. 5. While both consist of rings of six PO_4 tetrahedra, in O′-P_2O_5 the tetrahedra are organized in alternating rows along the [100] direction. Furthermore, in profile, O′-P_2O_5 resembles a sawtooth, whereas p-P_4O_{10} has the same waved appearance as phosphorene.

Nearly degenerate in energy with the planar p-P_4O_{10} form (Fig. 6), we find the tubular t-P_4O_{10} structure, shown in Fig. 4. The t-P_4O_{10} structure is a tubular (1D) form consisting of eight-member rings, connected to each other at an angle of approximately 100° (see, for example, the angle between the D′ and B′ bonds or D″ and C″ bonds in Fig. 4), these rings consisting of alternated phosphorus and bridging oxygen atoms. Only inversion symmetry is present, hence the space group is P^{-1} (C_i^1). There are two inequivalent (although very similar) PO_4 units, depicted in Fig. 4 (left side). The bond lengths and angles are listed in Table III.

TABLE III. Bond lengths and bond angles for p-P_4O_{10} and t-P_4O_{10} calculated with the PBE and PBEsol functionals. For the surface oxide forms, O-$P^{(\alpha)}$-$P^{(\beta)}$ is the angle between the O-$P^{(\alpha)}$ and the $P^{(\alpha)}$-$P^{(\beta)}$ bonds, where $P^{(\alpha)}$ and $P^{(\beta)}$ are nearest neighbors in the same zigzag ridge. Only inequivalent bonds are listed.

Planar form: p-P_4O_{10}

Bond lengths (Å)	PBE	PBEsol	Bond angles (°)	PBE	PBEsol
P=$O^{(A)}$	1.448	1.444	$O^{(A)}$-P-$O^{(B)}$	115.0	115.1
P–$O^{(B)}$	1.593	1.585	$O^{(A)}$-P-$O^{(C)}$	115.9	115.7
P–$O^{(C)}$	1.622	1.613	$O^{(A)}$-P-$O^{(D)}$	117.6	117.8
P–$O^{(D)}$	1.615	1.606			

Planar surface form: s-P_4O_2

Bond lengths (Å)	PBE	PBEsol	Bond angles (°)	PBE	PBEsol
P=$O^{(A)}$	1.482	1.477	O-$P^{(a)}$-$P^{(b)}$	108.8	104.1
P=$O^{(B)}$	1.477	1.516	O-$P^{(c)}$-$P^{(d)}$	107.3	111.8

Planar surface form: s-P_4O_4

Bond lengths (Å)	PBE	PBEsol	Bond angles (°)	PBE	PBEsol
P=$O^{(A)}$	1.474	1.468	O-$P^{(a)}$-$P^{(b)}$	111.2	111.3
P=$O^{(B)}$	1.507	1.510	O-$P^{(c)}$-$P^{(d)}$	109.9	110.8

Tubular form: t-P_4O_{10}

Bond lengths (Å)	PBE	PBEsol	Bond angles (°)	PBE	PBEsol
P=$O^{(A')}$	1.445	1.442	$O^{(A')}$-P-$O^{(B')}$	116.4	115.5
P–$O^{(B')}$	1.609	1.595	$O^{(A')}$-P-$O^{(C')}$	114.7	115.6
P–$O^{(C')}$	1.608	1.599	$O^{(A')}$-P-$O^{(D')}$	118.5	118.6
P–$O^{(D')}$	1.613	1.604			
P=$O^{(A'')}$	1.449	1.447	$O^{(A'')}$-P-$O^{(B'')}$	113.9	114.4
P–$O^{(B'')}$	1.603	1.588	$O^{(A'')}$-P-$O^{(C'')}$	115.3	115.0
P–$O^{(C'')}$	1.605	1.594	$O^{(A'')}$-P-$O^{(D'')}$	118.3	116.5
P–$O^{(D'')}$	1.607	1.599			

Similar to p-P_4O_{10}, t-P_4O_{10} can be seen as a corner-linked network of PO_4 tetrahedra. However, different from polyphosphate chains [42], in these tubular forms each tetrahedra shares three vertices, forming a tubular structure rather than a simple chain structure.

For intermediate concentrations, we find two metastable phosphorene oxides in which oxygen is present only on the phosphorene surface, in the form of dangling oxygen atoms. We refer to these as surface forms, and in particular as s-P_4O_2 for the single-surface oxidized and s-P_4O_4 for the double-surface oxidized; the two structures are shown in Fig. 1(c). As a result of oxygen chemisorption, the planes containing the top and the bottom zigzag ridges are not parallel to each other anymore (as in pristine phosphorene). The two P atoms in the same zigzag ridge are shifted from each other by about 0.5 Å in the direction perpendicular to the surface. In contrast with the other planar forms, the lattice deformation in this case is minimal.

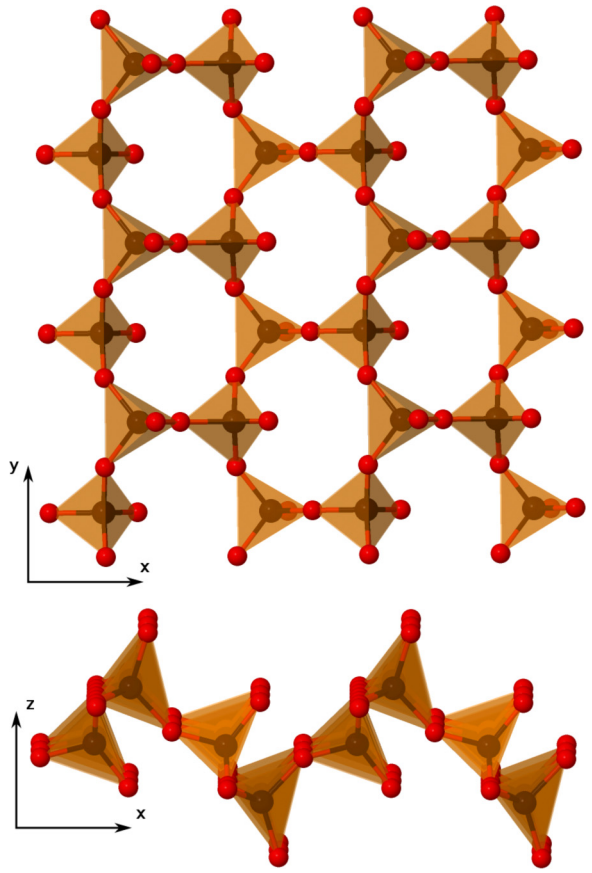

FIG. 5. (Color online) Crystal structure of single layer O′-P_2O_5.

B. Stability

The stability of the POs can be quantified by using the binding energy per oxygen atom, defined as [7]

$$E_b = -\frac{1}{N_O}\left[E_{ox} - \left(E_p + \frac{1}{2}N_O E_{O_2}\right)\right], \qquad (1)$$

where N_O is the number of O atoms in the unit cell, and E_{ox}, E_p, and E_{O_2} are the total energies of the PO, the pristine phosphorene, and the O_2 (triplet) molecule, respectively. From the definition above, a value of $E_b > 0$ indicates that the oxide formation is energetically favored in the presence of O_2. The average binding energies per O atom E_b for the most stable tubular, planar and surface POs calculated with the PBEsol and HSE functionals are shown in Fig. 6. The gain in energy due to oxygen chemisorption in phosphorene is very large across the whole concentration range (from ∼1.8 to 2.9 eV per O atom).

Regardless of the oxygen concentration, we invariably find that the lowest energy structure is a planar (p-P_4O_n) phosphorene oxide, with the tubular forms lying slightly higher in energy. In addition, for low and medium oxygen concentrations we find a manifold of states corresponding to different oxygen arrangements that have nearly the same energy.

For the lowest concentration considered, $n = 1$, the chemisorption of dangling oxygen is favored relative to bridging oxygens; in fact, p-P_4O_1 has a chemisorbed dangling oxygen ($E_b = 2.1$ eV), while on t-P_4O_1 we have a bridging oxygen ($E_b = 1.4$ eV). However, for all O concentrations higher than $n = 1$, no clear difference emerges in the energetics of dangling or bridging oxygens. The amount of energy gained after O chemisorption is dictated by the interplay between Coulomb repulsion of localized charges on the phosphorene surface and strain interactions, the former due to dangling oxygens and the latter mainly governed by bridging oxygens. Since bridging oxygens increase the P–P distance by about 0.7 Å [Fig. 2(b)], the insertion of oxygen bridges between neighboring dangling oxygens can substantially reduce their Coulomb repulsion, greatly stabilizing the PO. This explains the counterintuitive increase in binding energy per oxygen atom with increasing oxygen concentration.

The reduction of Coulomb repulsion due to the insertion of oxygen bridges is particularly evident for the case $n = 2$, shown in Fig. 7. Even though for $n = 1$ dangling oxygen chemisorption is favored over bridging oxygen chemisorption, when two dangling oxygens are chemisorbed on the same side of the phosphorene surface their strong Coulomb repulsion raises the energy of the compound, resulting in $E_b = 1.76$ eV for the surface form s-P_4O_2 (blue triangle at $n = 2$ in Fig. 6). This energy can be reduced by forming oxygen bridges instead of dangling oxygen, and therefore there are numerous other p-P_4O_2 and t-P_4O_2 forms containing bridging oxygen that are more stable (up to 1.02 and 0.74 eV, respectively) than s-P_4O_2. Similar considerations apply to the double-side surface oxidized form s-P_4O_4, which is ∼1.8 eV and ∼1.4 eV

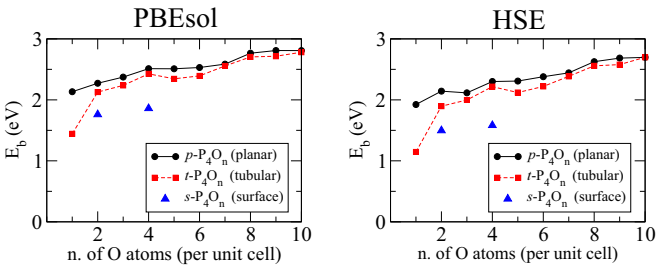

FIG. 6. (Color online) Average binding energy E_b per oxygen atom as a function of oxygen concentration calculated with the PBEsol and HSE functionals. Similar results are found for the PBE functional (shown in Supplemental Material). Black circles indicate planar PO forms (p-P_4O_n), red squares tubular forms (t-P_4O_n) and blue triangles surface forms (s-P_4O_n). The lines are a guide for the eye.

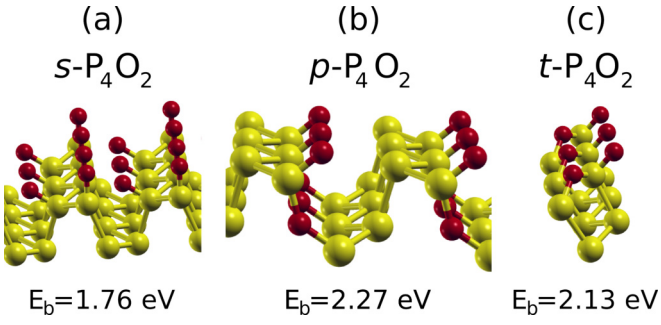

FIG. 7. (Color online) Different forms of phosphorene oxides and their average binding energy per oxygen atom E_b ($n = 2$).

higher in energy than the most stable planar and tubular forms, respectively, with the same concentration. From these simple considerations, we can argue that in near-equilibrium conditions the surface forms s-P_4O_2 and s-P_4O_4 will not be the primary outcome of phosphorene oxidation, contrary to what has been recently proposed [20,50]. Nevertheless, these surface oxidized forms can possibly be favored by specific kinetic factors. Still, since the activation energies for dangling oxygen formation and for oxygen insertion (bridges formation) are very similar (0.54 and 0.69 eV, respectively) [7], it is unlikely that these surface oxide phases will form even at low temperatures.

For the maximum oxygen concentration ($n = 10$), the p-P_4O_{10} and t-P_4O_{10} forms have nearly degenerate energies, with $E_b = 2.81$ eV (2.70 eV) and $E_b = 2.78$ eV (2.70 eV) at the PBEsol (HSE) level, respectively. They are nearly degenerate in energy with the O′ form, which has a binding energy of 2.81 eV with PBEsol (2.68 eV with HSE) in the monolayer form, or 2.88 eV (at the PBEsol level) in the bulk form. They also are the most stable POs among all O concentrations considered in this work. Their structures, which are essentially a homogeneous network of three-corner linked PO_4 tetrahedra (Figs. 3 and 4), minimize both strain interactions due to oxygen bridges and Coulomb repulsion from dangling oxygens.

C. Electronic properties

Chemisorption of oxygen atoms and the formation of POs drastically changes the electronic properties of phosphorene. The bandgap E_{gap} of both planar and tubular oxides is plotted as a function of oxygen concentration in Fig. 8. Both planar and tubular phosphorene oxides are found to be semiconducting or insulating, depending on the O concentration.

The bandgap of planar POs (black squares) increases monotonically with oxygen concentration, from 2.21 eV ($n = 1$) to 7.69 eV ($n = 10$) at the HSE level. Note that the bandgaps calculated at the PBEsol level follow almost precisely the same trends but are simply shifted to smaller gaps compared to HSE by roughly 1.5 eV across the entire O concentration range (see Fig. 8).

The increase in bandgap with O concentration in planar POs is due to the increasingly ionic character of the bonds and

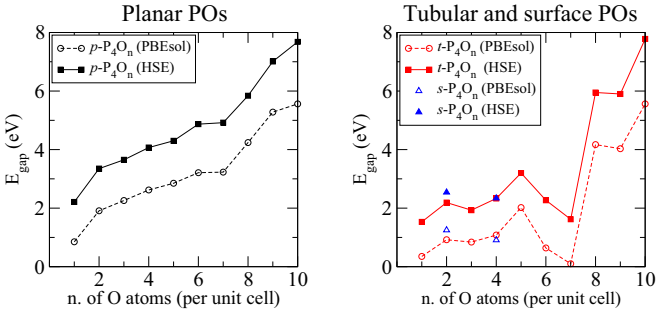

FIG. 8. (Color online) Bandgap energy E_{gap} calculated with the PBEsol and HSE functionals for planar (left panel), tubular and surface forms (right panel) as a function of oxygen concentration. The lines are a guide for the eye.

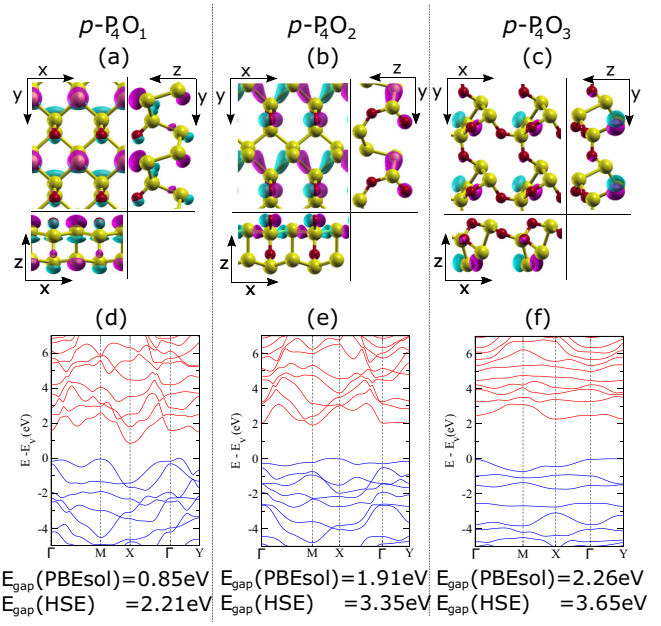

FIG. 9. (Color online) Crystal structure projections and valence band isosurface for low concentration planar POs: (a) p-P_4O_1, (b) p-P_4O_2, and (c) p-P_4O_3. The PBEsol electronic band structures are shown in panels (d)–(f), respectively. The top of the valence band is set to zero. The energy bandgaps at the PBEsol and HSE level are also given.

the resulting wave function localization. The series p-P_4O_n ($n = 1,2,3$), shown in Fig. 9 is a particularly instructive example of this phenomenon. In p-P_4O_1, one dangling oxygen is chemisorbed, corresponding to a 25% concentration. The band structure is strongly modified compared to pristine phosphorene (as shown in Supplemental Material [41]), but the valence band is still delocalized over all the crystal, as shown in Fig. 9(a), and still exhibits moderate dispersion. The bandgap is now indirect, but its value is still close to pristine phosphorene (2.21 eV vs 1.77 eV of pristine phosphorene at the HSE level in our calculation). If more oxygen atoms are added, the band structure drastically changes [Figs. 9(e)–9(f)]. In p-P_4O_2, the valence band becomes localized on the top zigzag ridge [Fig. 9(b)]. The valence band is now nearly completely flat, and the conduction band generally has less dispersion than that of p-P_4O_1. The bridging oxygen thus effectively creates nanoribbons and strongly increases the bandgap (3.35 eV with HSE). In p-P_4O_3 [Figs. 9(c)–9(f)] additional oxygen bridges, both intraridge and inter-ridge, are formed. The valence band is now localized on P, and both valence and conduction bands have very low dispersion due to their localization. The bandgap is 3.65 eV at the HSE level. For $n > 3$, all p-PO band structures preserve the low dispersion present in p-P_4O_3, together with an increasing bandgap. Their crystal structures and electronic band structures are shown in the Supplemental Material [41].

Tubular phosphorene oxides are also insulating, with bandgaps covering a large range of energies from 1.62 to 7.78 eV (at HSE level). In contrast to what we have described for planar POs, we did not find that tubular POs exhibit a monotonic increase in bandgap with oxygen concentration

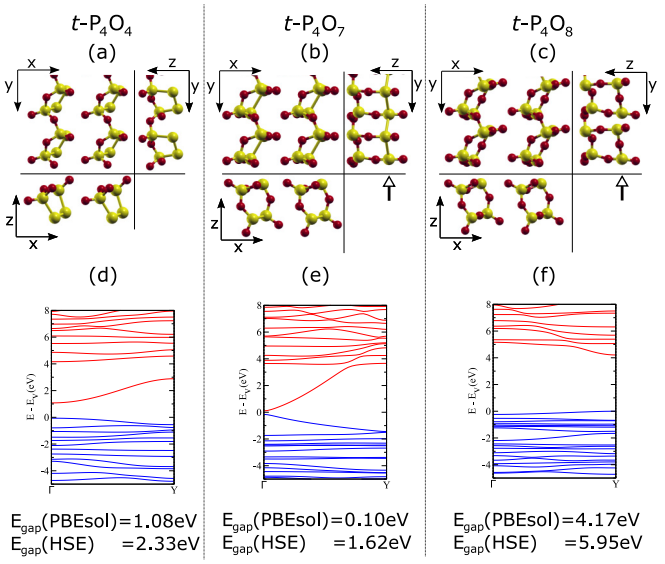

FIG. 10. (Color online) Crystal structure projections and conduction band isosurfaces for representative tubular POs: (a) t-P_4O_4, (b) t-P_4O_7, and (c) t-P_4O_8. The PBEsol electronic band structures are shown in panels (d)–(f), respectively. Only the dispersion along the 1D chains is shown. The top of the valence band is set to zero. The energy bandgaps at the PBEsol and HSE level are also given.

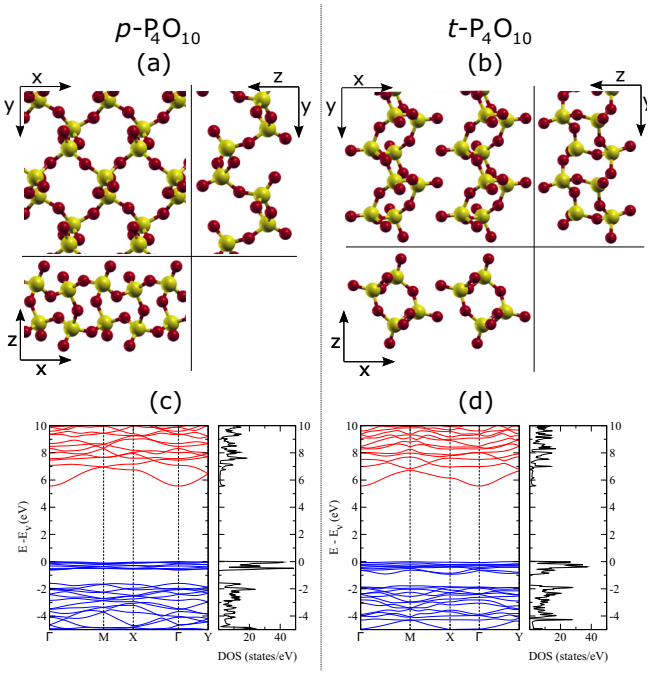

FIG. 11. (Color online) Crystal structures of oxygen saturated POs: (a) p-P_4O_{10} and (b) t-P_4O_{10}. The PBEsol electronic band structures are shown in panels (c) and (d), respectively. The top of the valence band is set to zero.

(see Fig. 8). We can separately consider two regimes, $n \leqslant 7$ and $n > 7$.

The crystal structure and electronic band structure of some representative tubular POs are shown in Fig. 10. The compound t-P_4O_4 [Fig. 10(a)] presents a feature common to all low- and medium-concentration tubular POs ($n \leqslant 7$): both occupied and unoccupied states around the Fermi energy are nearly flat, while the conduction band is dispersive and well separated from the manifold of occupied states (below) and empty states (above). The conduction band in this particular case has ∼2 eV bandwidth in all directions (Γ-M, M-X, and Γ-Y), but it is flat on the X-Γ direction, which is the direction perpendicular to the chain composing this tubular PO; this is the signature of the 1D nature of tubular POs. The strong Coulomb repulsion between dangling oxygens separates the chains, which interact only through (weak) van der Waals forces.

The compound t-P_4O_7 has a similar band structure, but shows increased dispersion of the conduction band [Figs. 10(b)–10(e)]. The conduction band arises from delocalized phosphorus p orbitals at the bottom of the PO layer, where no oxygen bridges are present [see right side of Fig. 10(b)]. The bandgap is only 1.62 eV (HSE level).

In the high-concentration regime ($n \geqslant 8$), the scenario is quite different. Chemisorption of a bridging oxygen atom in the phosphorus chain [marked by an arrow in Figs. 10(b) and 10(c)] breaks the conjugation, localizing both conduction and valence bands, and greatly increasing E_{gap}. This is particularly evident in t-P_4O_8 [Figs. 10(c)–10(f)]: the conduction band, in contrast to the situation discussed above, is now very close to the manifold of unoccupied states and presents no dispersion. The bandgap increases by roughly ∼4 eV at both PBEsol and HSE levels, making the material an insulator. The surface forms s-P_4O_2 and s-P_4O_4 are instead both semiconducting with HSE bandgaps of 2.54 and 2.34 eV, respectively.

The electronic band structure and the density of states (DOS) of the maximally oxidized phosphorene oxides p-P_4O_{10} and t-P_4O_{10} are shown in Fig. 11.

Both POs are insulators, and they have remarkably similar band structures. There is a manifold of eight nearly degenerate dispersionless occupied states between −1 and 0 eV for both species; these states are p orbitals localized on dangling oxygens, bridging oxygens or both, and they do not have any appreciable electron density on the P atoms. The conduction band consists instead of p orbitals on dangling oxygens and on P-O bridges, and it is slightly dispersive. The bandgap is 5.56 eV for both species at the PBEsol level, enlarged at 7.68 eV for p-P_4O_{10} and at 7.78 eV for t-P_4O_{10} with the HSE functional. Interestingly, we find that monolayer O′-P_2O_5 has a similar HSE bandgap (7.45 eV).

For pristine phosphorene and the maximally oxidized phosphorene oxides we calculated the bandgaps also within the GW approximation [35,36]. For the pristine phosphorene we obtain 1.70 eV, close to the 1.60 eV of Ref. [51], but different by 0.3 eV from Tran *et al.* [2]. We note that all the convergence parameters used in this work are higher than those used in these previous studies (see Supplemental Material for a complete comparison [41]).

For p-P_4O_{10} and t-P_4O_{10} we obtain GW bandgaps of 8.50 and 8.69 eV, respectively, close to the HSE results. The bandgaps for pristine phosphorene and maximal oxidation POs calculated with different levels of theory are summarized in Table IV.

TABLE IV. Energy bandgaps for pristine phosphorene and maximal oxidation POs.

System	E_{gap} (eV)		
	PBEsol	HSE	*GW*
Phosphorene	0.72	1.77	1.70
p-P_4O_{10}	5.56	7.68	8.50
t-P_4O_{10}	5.56	7.78	8.69

D. Vibrational properties

Even though the Raman spectrum of POs changes quite significantly depending on the oxygen concentration, it is possible to identify three distinctive vibrational bands common throughout the whole P_4O_n series. Some of the typical vibrational modes relevant in these different regions are presented in Fig. 12. The low-frequency region of the vibrational spectra (<300 cm^{-1}) is dominated by the wag modes of the P=O groups, mixed with a small component of P-O-P bending. The presence of P-O-P bending modes increases with frequency and becomes strongly predominant in the region between 500 and 1000 cm^{-1}. For the surface forms (s-P_4O_2 and s-P_4O_4) in which only dangling oxygens are present, there are indeed no vibrational modes between 500 and 1000 cm^{-1}. In the high-frequency region, the vibrational spectrum instead only involves P=O stretching modes; these modes are decoupled from the other vibrations because the P=O bonds are much stronger than P-O bridges, as in the case of the molecular (bulk) phosphorus oxides [52,53]. The P=O stretching modes are separated from the other modes by at least 200 cm^{-1} for all oxygen concentrations, and there are as many as the number of dangling oxygen in the PO. This observation opens the possibility of direct experimental detection of the number of dangling oxygens through Raman spectroscopy. P=O stretching modes start at 1063 cm^{-1} for $n = 1$ (p-P_4O_1) and monotonically blueshift with increasing oxygen concentration till about ~1370 cm^{-1} for maximum oxidation. This is consistent with the shortening of P=O bond found with increasing oxygen linkage, as shown in Table I and analogous to the observed blueshift of P=O vibrational frequencies in the series P_4O_m (m = 6 to 10) measured in solid argon [54].

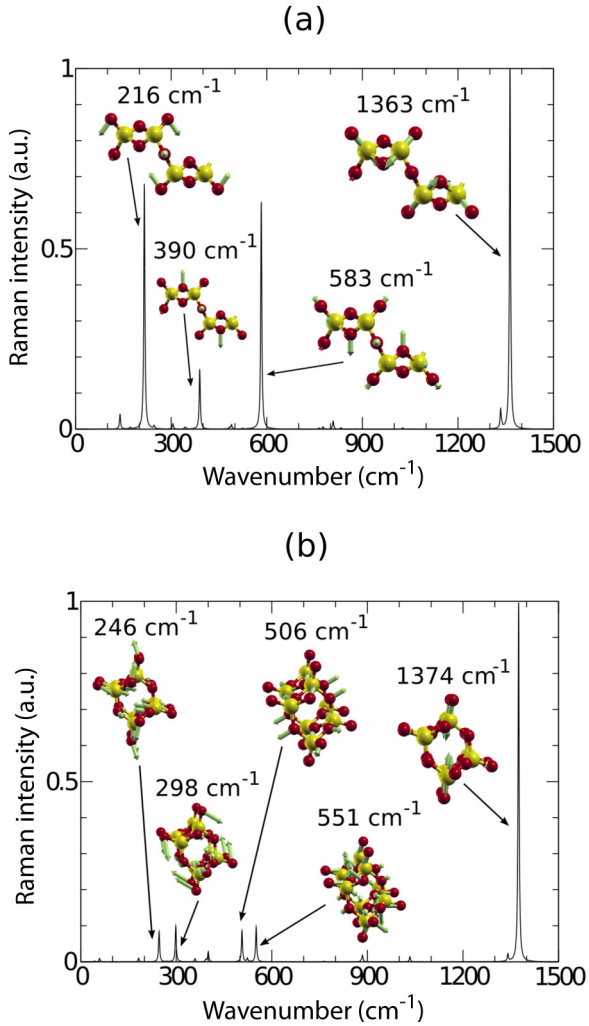

FIG. 12. (Color online) Raman spectra and corresponding Raman active modes for (a) p-P_4O_{10} and (b) t-P_4O_{10}. The length of the arrows is proportional to the amplitude of motion.

Raman spectra and Raman active modes of p-P_4O_{10} and t-P_4O_{10} are shown in Figs. 12(a) and 12(b), respectively. In p-P_4O_{10}, there are three high-intensity Raman peaks at 216, 583, and 1363 cm^{-1} and a low-intensity peak at 390 cm^{-1}. The first peak (216 cm^{-1}) consists of the concerted wag mode of the four P=O dangling oxygens (scissoring), together with an symmetric P-O-P stretch of the two inter-ridge bridges [purple in Fig. 3(b)]. The second strong peak at 583 cm^{-1} is a combination of the P-O-P symmetric stretch of the middle intraridge bridges [brown in Fig. 3(b)] and the P=O stretch of all dangling oxygens. The last strong peak (1363 cm^{-1}) involves the stretching of the P=O bonds. The low-intensity peak at 390 cm^{-1} is instead the P-O-P symmetric stretching of the lower and higher intraridge bridges [gray in Fig. 3(b)].

In contrast, only one strong peak at 1374 cm^{-1}, corresponding to the P=O stretching of two dangling oxygens, is present in the Raman spectrum of t-P_4O_{10}, as shown in Fig. 12(b). Four low-intensity peaks, however, appear in the range 250–550 cm^{-1}.

The mode at 246 cm^{-1} involves P=O bond scissoring with a contribution from an asymmetrical bending of the P-O-P bridges, while the one at 298 cm^{-1} involves P=O scissoring such that the top and bottom layer dangling oxygen moves towards the tubular oxide center. Finally, at 506 cm^{-1} we find a ring-breathing mode (P-O-P symmetrical bending of inter-ridge bridges) and at 551 cm^{-1} another ring breathing mode plus P=O stretching.

Raman and IR spectra for planar and tubular forms for all oxygen concentrations are reported in the Supplemental Material [41].

IV. CONCLUSIONS

We have described a family of two-dimensional phosphorus oxides obtained by oxidation of phosphorene, with oxygen content up to ten oxygen per phosphorene unit cell (P_2O_5).

The gain in energy due to oxygen chemisorption in phosphorene is very large (from ~1.8 to 2.9 eV per O

atom) and increases with the oxygen concentration. In parallel with the two-dimensional planar forms, there are tubular (polymeric) forms with similar formation enthalpy. The planar forms are lower in energy than the tubular forms for all O concentrations; the energy difference is, however, quite small (typically <0.1 eV per O atom), hence both forms are likely to coexist under normal experimental conditions, forming ordered and disordered (amorphous) domains depending on the oxidation process, local impurities, and defects. It is also feasible that different forms of POs can be experimentally created by a suitable choice of growth conditions, in much the same way as the (bulk) series P_4O_{6+m} ($0 \leqslant m \leqslant 4$) can be obtained by varying the atmosphere, temperature, and pressure in which P_4 is treated [42,44]. Moreover, both planar and tubular forms have the very similar formation enthalpy of the thermodynamically most stable known phosphorus pentoxide (O'-P_2O_5).

The phosphorene oxides can be used as a transparent tunneling materials; namely, on black-phosphorus or phosphorene-based devices. The bandgap energy of planar P_4O_n increases with n and is 8.5 eV for $n = 10$. The tubular forms are also insulating and, close to the oxygen-saturation limit (P_2O_5), have nearly the same gap energy, and therefore their coexistence with the planar form does not jeopardize its transparency or electrical insulation properties.

Although the planar and the tubular form of P_2O_5 give rise to high-frequency Raman scattering peaks with very close energies (at 1363 and 1374 cm^{-1}), the planar form can be identified by an intense peak at 583 cm^{-1}, just above the Raman edge of black phosphorus (470 cm^{-1} at room temperature [55]). Additionally, the Raman spectra can supply information on the oxygen concentration and, for a crystalline sample, on the number of dangling oxygen per unit cell.

ACKNOWLEDGMENTS

A.Z. and D.F.C. acknowledge National Science Foundation grant CHE-1301157 and also an allocation of computational resources from Boston University's Office of Information Technology and Scientific Computing and Visualization. A.Z. also acknowledges the support from grant CMMI-1036460, Banco Santander. A.H.C.N., A.C. and P.E.T. acknowledge the National Research Foundation, Prime Minister's Office, Singapore, under its Medium Sized Centre Programme and Competitive Research Program award "Novel 2D materials with tailored properties: beyond graphene" (R-144-000-295-281).

[1] A. S. Rodin, A. Carvalho, and A. H. Castro Neto, Phys. Rev. Lett. **112**, 176801 (2014).
[2] Vy Tran, Ryan Soklaski, Yufeng Liang, and Li Yang, Phys. Rev. B **89**, 235319 (2014).
[3] Q. Wei, and X. Peng, Appl. Phys. Lett. **104**, 251915 (2014).
[4] S. P. Koenig, R. A. Doganov, H. Schmidt, A. H. Castro Neto, and B. Ozyilmaz, Appl. Phys. Lett. **104**, 103106 (2014).
[5] F. Xia, H. Wang, and Y. Jia, Nat. Commun. **5**, 4458 (2014).
[6] M. Buscema, D. J. Groenendijk, S. I. Blanter, G. A. Steele, H. S. J. van der Zant, and A. Castellanos-Gomez, Nano Lett. **14**, 3347 (2014).
[7] A. Ziletti, A. Carvalho, D. K. Campbell, D. F. Coker, and A. H. Castro Neto, Phys. Rev. Lett. **114**, 046801 (2015).
[8] R. A Doganov, E. C. T. O'Farrell, S. P. Koenig, Y. Yeo, A. Ziletti, A. Carvalho, D. K. Campbell, D. F. Coker, K. Watanabe, T. Taniguchi, A. H. Castro Neto, and B. Ozyilmaz, arXiv:1412.1274.
[9] A. Castellanos-Gomez, L. Vicarelli, E. Prada, J. O. Island, K. L. Narasimha-Acharya, S. I. Blanter, D. J. Groenendijk, M. Buscema, G. A. Steele, J. V. Alvarez, H. W. Zandbergen, J. J. Palacios, and H. S. J. van der Zant, 2D Mater. **1**, 025001 (2014).
[10] J. O. Island, G. A. Steele, H. S. J. van der Zant, and A. Castellanos-Gomez, 2D Mater. **2**, 011002 (2015).
[11] A. Favron, E. Gaufrès, F. Fossard, P. L. L'evesque, A-L. Phaneuf-L'Heureux, N. Y.-W. Tang, A. Loiseau, R. Leonelli, S. Francoeur, and R. Martel, arXiv:1408.0345.
[12] S. Yau, T. P. Moffat, A. J. Bard, Z. Zhang, and M. M. Lerner, Chem. Phys. Lett. **198**, 383 (1992).
[13] T. W. Farnsworth, R. A. Wells, A. H. Woomer, J. Hu, C. Donley, and S. C. Warren, Informal Phosphore Symposium (2014).
[14] R. K. Brow, J. Non-Cryst. Solids **263-264**, 1 (2000).
[15] B. Jansen and M. Luer, Z. Kristallogr. **177**, 149 (1986).
[16] E. H. Arbib, B. Elouadi, J. P. Chaminade, and J. Darriet, J. Solid State Chem. **127**, 350 (1996).
[17] D. Stachel, I. Svoboda, and H. Fuess, Acta Crystallogr., Sect. C: Cryst. Struct. Commun. **51**, 1049 (1995).
[18] F. Hulliger, *Structural Chemistry of Layer-Type Phases*, edited by F. Lévy (D. Reidel publishing company, Dordrecht, Holland, Boston, USA, 1976).
[19] F. L. Galeener, and J. C. Mikkelsen Jr, Solid State Commun. **30**, 505 (1979).
[20] G. Wang, R. Pandey, and S. P. Karna, Nanoscale **7**, 524 (2015).
[21] P. Giannozzi *et al.*, J. Phys.: Condens. Matter **21**, 395502 (2009).
[22] J. P. Perdew, K. Burke, and M. Ernzerhof, Phys. Rev. Lett. **77**, 3865 (1996).
[23] J. P. Perdew, A. Ruzsinszky, G. I. Csonka, O. A. Vydrov, G. E. Scuseria, L. A. Constantin, X. Zhou, and K. Burke, Phys. Rev. Lett. **100**, 136406 (2008).
[24] Aliaksandr V. Krukau, Oleg A. Vydrov, Artur F. Izmaylov, and Gustavo E. Scuseria, J. Chem. Phys. **125**, 224106 (2006).
[25] J. Heyd, J. E. Peralta, G. E. Scuseria, and R. L. Martin, J. Chem. Phys. **123**, 174101 (2005).
[26] B. G. Janesko, T. M. Henderson, and G. E. Scuseria, Phys. Chem. Chem. Phys. **11**, 443 (2009).
[27] T. M. Henderson, J. Paier, and G. E. Scuseria, Phys. Status Solidi B **248**, 767 (2011).
[28] P. E. Blöchl, Phys. Rev. B **50**, 17953 (1994).
[29] N. Troullier and J. L. Martins, Phys. Rev. B **43**, 1993 (1991).
[30] S. Baroni, S. de Gironcoli, A. Dal Corso, and P. Giannozzi, Rev. Mod. Phys. **73**, 515 (2001).
[31] H. J. Monkhorst and J. D. Pack, Phys. Rev. B **13**, 5188 (1976).
[32] P. E. Blöchl, O. Jepsen, and O. K. Andersen, Phys. Rev. B **49**, 16223 (1994).

[33] J. P. Perdew, R. G. Parr, M. Levy, and J. L. Balduz, Phys. Rev. Lett. **49**, 1691 (1982).
[34] J. P. Perdew and M. Levy, Phys. Rev. Lett. **51**, 1884 (1983).
[35] L. Hedin, Phys. Rev. **139**, A796 (1965).
[36] M. S. Hybertsen and S. G. Louie, Phys. Rev. B **34**, 5390 (1986).
[37] S. G. Louie, in *Topics in Computational Materials Science*, edited by Ching-Yao Fong (World Scientific, Singapore, 1998), p. 96.
[38] B. D. Malone and M. L. Cohen, J. Phys.: Condens. Matter **25**, 105503 (2013).
[39] S. Ismail-Beigi, Phys. Rev. B **73**, 233103 (2006).
[40] X. Gonze *et al.*, Comput. Phys. Commun. **180**, 2582 (2009).
[41] See Supplemental Material at http://link.aps.org/supplemental/10.1103/PhysRevB.91.085407 for details of convergence in the *GW* calculations; electronic band structure of pristine phosphorene; crystal structure, electronic band structure, Raman and IR spectra for planar and tubular phosphorene oxides.
[42] N. N. Greenwood and A. Earnshaw, *Chemistry of the Elements* (Pergamon Press, New York, 1984).
[43] Oftentimes this bond is classified as a double bond [19,42,56,57], although its identification as P=O is not commonly accepted [58–60]. Nevertheless, hereafter we will refer to this bond as P=O for simplicity.
[44] M. Jansen, M. Voss, and H. J. Deiseroth, Angew. Chem., Int. Ed. Engl. **20**, 965 (1981).
[45] M. L. Walker, D. E. Peckenpaugh, and J. L. Mills, Inorg. Chem. (Washington, DC, U.S.) **18**, 2792 (1979).
[46] J. Clade, F. Frick, and M. Jansen, Adv. Inorg. Chem. **41**, 327 (1994).
[47] R. J. Gillespie and R. S. Nyholm, Q. Rev., Chem. Soc. **11**, 339 (1957).
[48] R. J. Gillespie, J. Chem. Educ. **40**, 295 (1963).
[49] R. J. Gillespie, Chem. Soc. Rev. **21**, 59 (1992).
[50] J. Daia and X. C. Zenga, RSC Adv. **4**, 48017 (2014).
[51] A. N. Rudenko and M. I. Katsnelson, Phys. Rev. B **89**, 201408 (2014).
[52] A. R. S. Valentim, B. Engels, S. Peyerimhoff, J. Clade, and M. Jansen, Inorg. Chem. (Washington, DC, U.S.) **36**, 2451 (1997).
[53] A. R. S. Valentim, B. Engels, S. D. Peyerimhoff, J. Clade, and M. Jansen, J. Phys. Chem. A **102**, 3690 (1998).
[54] Z. Mielke and L. Andrews, J. Phys. Chem. **93**, 2971 (1989).
[55] S. Sugai and I. Shirotani, Solid State Commun. **53**, 753 (1985).
[56] F. L. Galeener, J. C. Mikkelsen, Jr., R. H. Geils, and W. J. Mosby, Appl. Phys. Lett. **32**, 34 (1978).
[57] V. V. Brazhkin, J. Akola, Y. Katayama, S. Kohara, M. V. Kondrin, A. G. Lyapin, S. G. Lyapin, G. Tricot, and O. F. Yagafarov, J. Mater. Chem. **21**, 10442 (2011).
[58] D. G. Gilheany, Chem. Rev. (Washington, DC, U.S.) **94**, 1339 (1994).
[59] U. S. Rai and M. C. R. Symons, J. Chem. Soc., Faraday Trans. **90**, 2649 (1994).
[60] D. B. Chesnut and A. Savin, J. Am. Chem. Soc. **121**, 2335 (1999).